Journal of Power Sources 193 (2009) 665–683

Contents lists available at ScienceDirect

Journal of Power Sources

journal homepage: www.elsevier.com/locate/jpowsour

A generalized numerical model for liquid water in a proton exchange membrane fuel cell with interdigitated design

Anh Dinh Le, Biao Zhou*

Department of Mechanical, Automotive & Materials Engineering, University of Windsor, ON, Canada N9B 3P4

ARTICLE INFO

Article history:
Received 20 February 2009
Received in revised form 7 April 2009
Accepted 9 April 2009
Available online 18 April 2009

Keywords:
PEM fuel cell
CFD
Interdigitated channel
Two-phase flow
Volume of fluid
Water management

ABSTRACT

A new approach to numerical simulation of liquid water distribution in channels and porous media including gas diffusion layers (GDLs), catalyst layers, and the membrane of a proton exchange membrane fuel cell (PEMFC) was introduced in this study. The three-dimensional, PEMFC model with detailed thermo-electrochemistry, multi-species, and two-phase interactions. Explicit gas–liquid interface tracking was performed by using Computational Fluid Dynamics (CFD) software package FLUENT® v6.2, with its User-Defined Functions (UDF) combined with volume-of-fluid (VOF) algorithm. The liquid water transport on a PEMFC with interdigitated design was investigated. The behavior of liquid water was understood by presenting the motion of liquid water droplet in the channels and the porous media at different time instants. The numerical results show that removal of liquid water strongly depends on the magnitude of the flow field. Due to the blockage of liquid water, the gas flow is unevenly distributed, the high pressure regions takes place at the locations where water liquid appears. In addition, mass transport of the species and the current density distribution is significantly degraded by the presence of liquid water.

1. Introduction

Actual PEMFC operation is a complex process including transport of mass, momentum, energy, species and charges that take place simultaneously. Furthermore, a PEMFC is a multi-part device that comprises of collectors, flow channels, GDLs, catalyst layers and the PEM membrane. During a PEMFC operation, hydrogen is consumed in the anode; oxygen is consumed and water is produced in the cathode; and a current is generated from anode side to cathode side via electric load. Water product exists in the forms of water vapor and/or liquid water depending on physical conditions such as pressure, temperature, etc., leading to a gas–liquid flow in the porous media and the channels. Such water significantly influences the fuel cell operation and performance as well: water content increases ionic conductivity of the membrane, leading to a high current density in a specific volume of the cell; liquid water may block the gas transport inside the channel and porous media and cause flooding phenomenon and therefore, decreasing the cell performance. Therefore, water management, especially liquid water management, to which many engineers and scientists have recently paid particular attention, has been a critical challenge for high-performance fuel cell design and optimization.

In order to fully understand physical and electrochemical processes occurring in a PEMFC, and especially water management, numerical modeling is a strong method that has been much considered in recent years. As mentioned above, PEMFC operation involves simultaneous, complex processes and hence, the development of 3-D models for a complete PEMFC that considers all parts, all components and all phenomena is a big challenge. Fortunately, with the developments of high performance computing and advanced numerical algorithms, it has allowed researchers to model PEMFC systems as well as individual components with greater fidelity than ever before. Recently, three-dimensional Computational Fluid Dynamics (CFD) models have been developed by taking full advantage of different commercial CFD software packages such as Fluent®, CFX®, Star-CD®, and CFDRC®, etc. Typical models that simultaneously considered the electrochemical kinetics, current distributions, fluid dynamics, and multi-component transport accounted for single-phase and two-phase were conducted by Wang and co-workers [1–4]. In these studies, liquid water saturation was addressed to characterize the two-phase flow in the cathode channel and cathode GDL. The CFD software Fluent was also used to simulate fluid flow in PEMFC channel by Dutta et al. [5] or predict liquid water saturation with experimentally measured capillary functions by Ye and Nguyen [6]. Djilali et al. presented a multi-phase, multi-component 3-D model with heat and mass transfer, where liquid water transport in GDLs was numerically presented [7,8]. Another model to treat liquid water formation and transport in a PEMFC was introduced by Mazumder and Cole [9]. Other approach to deal with two-phase flow in GDLs based on thermodynamic equilibrium conditions was given by Vynnycky [10]. By using this approach, the location of the interface between

* Corresponding author. Tel.: +1 519 253 3000x2630; fax: +1 519 973 7007.
E-mail address: bzhou@uwindsor.ca (B. Zhou).

0378-7753/$ – see front matter © 2009 Elsevier B.V. All rights reserved.
doi:10.1016/j.jpowsour.2009.04.011

Nomenclature

a	water activity, dimensionless
A_{surf}	reactive surface area, m^2
A_s	heat transfer surface area, m^2
c_p	specific heat capacity, $J\,kg^{-1}\,K^{-1}$
C_i	species concentration i, $kmol\,m^{-3}$
D_i	diffusion coefficient of species i in gas mixture, $m^2\,s^{-1}$
F	Faraday constant, 9.6487×10^7 C kmol^{-1}
h	convective heat transfer, $W\,m^{-2}\,K^{-1}$
h_{H_2O}	the enthalpy of formation of water vapor, $N\,m\,kg^{-1}$
I	current density, $A\,m^{-2}$
I_{ave}	average current density, $A\,m^{-2}$
J	mass flux, $kg\,m^{-2}\,s^{-1}$
k_{eff}	effective thermal conductivity, $W\,m^{-1}\,K^{-1}$
M_i	molecular weight of species i in gas mixture, $kg\,kmol^{-1}$
n_d	electro-osmotic drag coefficient, dimensionless
n_f	charge number of the sulfonic acid ion
P	pressure, Pa
P_i	partial pressure of species i, Pa
R	universal gas constant, $8314\,J\,kmol^{-1}\,K^{-1}$
$\dot{Q}$	heat rate, W
R_{cat}, R_{an}	volumetric current density, $A\,m^{-3}$
S	source term
t	time, s
T	temperature, K
u, v, w	velocities in x, y, and z directions, respectively, $m\,s^{-1}$
V_{oc}	open-circuit potential, V
V_{cell}	cell potential, V
V_{ref}	reference potential, V
$\forbar{V}$	volume, m^3
X_i	mole fraction of species i, dimensionless
Y_i	mass fraction of species i, dimensionless

Greek symbols

α	transfer coefficient,
β	the factor accounts for energy release
ε	porosity
ϕ	phase potential, V
γ	concentration dependence
γ_p, γ_T	exponent factors
η	overpotential, V
φ	relative water content
κ	surface curvature
τ_g	gaseous permeability, m^2
τ_l	liquid permeability, m^2
τ_p	hydraulic permeability, m^2
τ_ϕ	electrokinetic permeability, m^2
λ	water content
μ	dynamic viscosity, $kg\,m^{-2}\,s^{-1}$
ρ	density of gas mixture, $kg\,m^{-3}$
ρ_i	density of species i, $kg\,m^{-3}$
σ	phase conductivity, $\Omega^{-1}\,m^{-1}$
υ	reaction rate, $kmol\,m^2\,s^{-1}$
ω	excess coefficient
χ	surface tension coefficient, $N\,m^{-1}$
θ_w	contact angle, °

Subscripts and superscripts

an	anode
cat	cathode
e	electrochemical reaction
eff	effective
g	gas phase
H_2	hydrogen
H_2O	water
i	species i
in	inlet
l	liquid phase
m	membrane phase
out	outlet
N_2	nitrogen
O_2	oxygen
ref	reference
s	solid phase
sat	saturated
surf	surface
w	water vapor

one phase and the other phase was discovered from its numerical results.

Two-phase flow models that account for liquid water formation in the porous media including GDLs and catalyst layers were developed in several ways. A typical approach using the network model to investigate the effective diffusivity and water saturation was developed early by Nam and Kaviany [11]. In this study, the effects of the fiber diameter, porosity, and capillary pressure on the water saturation and the cell performance are also presented. The effective permeability and capillary pressure in porous GDLs were also addressed by using capillary pore network simulations given by Djilali et al. [12]. Consequently, the pore network method has been used to address the liquid water behavior in a PEMFC by Fowler and co-workers [13], Prat and co-workers [14], and Pasaogullari and Wang [15].

A new, comprehensive approach used to address the behavior of liquid water transport inside PEMFCs was early developed by Zhou and co-workers [16–18] that considers volume-of-fluid (VOF) interface tracking between liquid water and gas. This study also conducted two more studies that dealt with liquid water in serpentine and straight parallel fuel cell stacks. The results showed that different designs of gas diffusion layers (GDLs) and flow channels will affect the liquid water flow patterns significantly, thus influencing the performance of PEMFCs. In recent years, Djilali and co-workers [19] presented a 2-D, numerical investigation of the dynamic behavior of liquid water entering a PEMFC channel through a small hole that was assumed as a GDL pore. The 3-D simulation models focusing on characteristics of water droplets and water film motion in the flow channels and/or GDL were also developed by using VOF method by Djilali and co-workers [20,21] Zhan et al. [22], Quan and Lai [23], Golpaygan and Ashgriz [24].

In these studies, the water behavior can be investigated, giving very useful insights about water management in the channels, however the electrochemical reactions and the effects of liquid water on mass and heat transport that take place in an actual PEMFC have not been considered.

Therefore, a general 3-D PEMFC model including the entire serpentine flow channels, GDLs, catalyst layers, membrane and collectors all with detailed physics included (e.g., multi-phase with VOF interface-tracking between gas-phase and liquid-water-phase, multi-components, heat and mass transfer, electrochemical reactions, and water-phase-change effects) has been developed by Le and Zhou [25]. In this study, as a pioneering work in this research area, the mathematical model is applied to a PEMFC with interdigitated flow channels. A unified method is used to treat the transport of water in different zones: the species transport equation of water

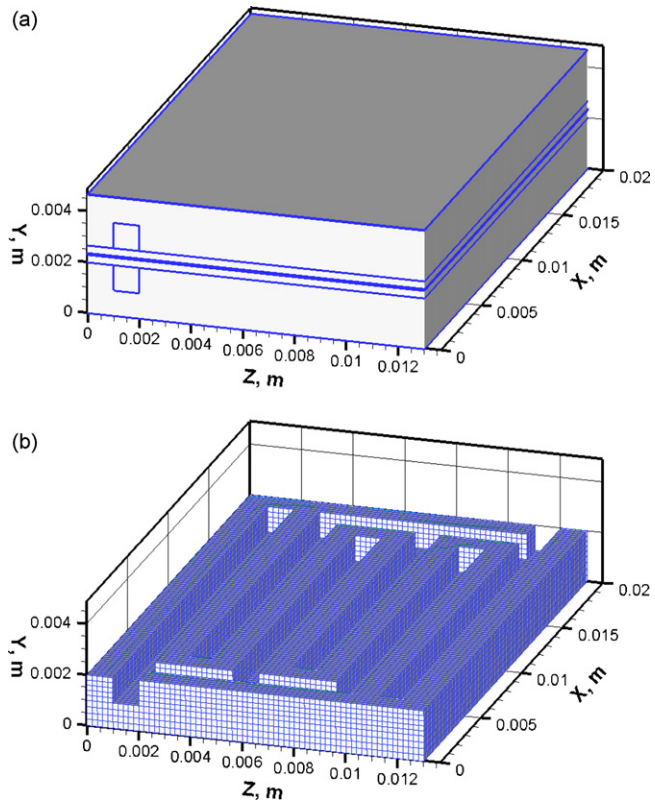

Fig. 1. (a) Schematic diagram of the PEMFC and (b) geometry and computational mesh of the interdigitated channel.

vapor coupled with the water transport through the membrane (including the electro-osmotic drag and the back diffusion effects) is used for different zones with different source terms. Furthermore, we also use VOF method to track liquid water and treat water vapor as one of the gaseous species. By this way, liquid water motion and behavior inside the porous media are implicitly investigated in the flow interdigitated channel with baffles. The simulation results would provide an in-depth understanding of liquid water transport and its effects on fuel cell performance in an interdigitated flow-field PEMFC.

2. Mathematical model

Fig. 1 shows schematic structure of the 3-D PEMFC used in this study. The mathematical model considers all the parts shown in Fig. 1a, the computation grid of interdigitated channel is shown in part b, with geometrical parameters listed in Table 1. The computation domain consists of current collectors, flow channels, GDLs, catalyst layers and the membrane. The channels are interdigitated.

2.1. Model assumptions

The assumptions used in developing the model are:

1. Ideal gas law was employed for gaseous species.
2. The fluid flow in the fuel cell was laminar due to the low flow velocities and the small size of gas flow channels.
3. The porous media including membrane, catalyst layers and GDLs were considered to be isotropic.
4. The fuel cell cooling was controlled by forced convection heat transfer.

Table 1
Geometrical properties and operation conditions.

Physical properties or parameters	Value
Channel width	0.001 m
Channel height	0.001 m
Membrane thickness	50×10^{-6} m
GDL thickness	300×10^{-6} m
Catalyst layer thickness	10×10^{-6} m
Anode and Cathode Inlet Temperature	300 K
Anode inlet excess coefficient, ω_a	3
Cathode inlet excess coefficient, ω_c	3
Open-circuit voltage, V_{oc}	1.15 V
Gas Constant, R	8.314 J kmol^{-1} K^{-1}
Anode exchange current density/reference hydrogen concentration, $R_{an}^{ref}/(C_{H_2}^{ref})^{\gamma an}$	7×10^{10} A kmol^{-1}
Cathode exchange current density/reference oxygen concentration, $R_{cat}^{ref}/(C_{O_2}^{ref})^{\gamma cat}$	7×10^{5} A kmol^{-1}
Anode transfer coefficient, α_{an}	0.5
Cathode transfer coefficient, α_{cat}	0.5
Anode concentration dependence, γ_{an}	0.5
Cathode concentration dependence, γ_{cat}	1.0
Factor accounts for energy release, β	0.5
Membrane porosity, ε_{mem}	0.5
Diffusion layer porosity, ε_{gdl}	0.5
Catalyst layer porosity, $\varepsilon_{catalyst}$	0.5
Permeability of porous media, τ	1.76×10^{-11} m^2
Contact angle, θ_w	90°
Surface tension, χ	0.065 N m^{-1}

2.2. Governing equations

In this study, the PEMFC model includes the principles of conservation: mass and momentum for solving fluid flow, energy for solving heat generation and transfer, species for solving species transport, and charge for solving current density distribution. In addition, a volume fraction equation was used to track gas–liquid interfaces. These governing equations are presented in the following forms:

Continuity and momentum equations

$$\frac{\partial \varepsilon\rho}{\partial t} + \nabla \cdot (\varepsilon\rho\vec{v}) = S_m \quad (1)$$

$$\frac{\partial}{\partial t}(\varepsilon\rho\vec{v}) + \nabla(\varepsilon\rho\vec{v}\vec{v}) = -\varepsilon\nabla p + \nabla[\varepsilon\mu\nabla\vec{v}] + S_v \quad (2)$$

The source terms for the continuity and momentum equation used in the model for different regions of the fuel cell are given in Table 2. For the different fluid zones, different source terms are used to describe the flow of the fluid through a porous media by using viscous loss—Darcy's drag force [26]. In addition, the gravity and surface tension forces were also considered in the momentum equation source term.

Mixture properties: The gas and liquid phases are considered as a two-phase mixture flow. For the mixture flow including gas and liquid, the volume fractions of the gas and liquid phases in the computational cell are introduced. In each control volume, the sum of volume fractions of two phases is unity. Then, mixture properties are defined as in Table 3.

Volume fraction equation of liquid water

$$\frac{\partial}{\partial t}(\varepsilon s_l\rho_l) + \nabla(\varepsilon s_l\rho_l\vec{v}_l) = S_s \quad (3)$$

The tracking of the interface between the phases was accomplished by the solution of a continuity equation for the volume fraction of one (or more) of the phases. The motion of the interface between two immiscible liquids (namely, the gas and liquid water) of different density and viscosity in the VOF method was defined by volume fraction of liquid water s_l and volume fraction of the gaseous phase s_g [26]. In this model, the volume fraction equation

Table 2
The source terms of governing equations.

Governing equation	Volumetric source terms and location of application
Conservation of mass	For gas channels, GDL and the membrane $S_m = 0$ For anode catalyst layer: $S_m = -\frac{M_{H_2}}{2F} R_{an} - \left(\frac{n_d M_{H_2O}}{F}\right) R_{an}$ For cathode catalyst layer: $S_m = -\frac{M_{O_2}}{4F} R_{cat} + \frac{M_{H_2O}}{2F} R_{cat} + \left(\frac{n_d M_{H_2O}}{F}\right) R_{cat}$
Volume fraction	For all parts: $S_s = r_w$
Conservation of momentum	For gas channels: $S_v = 0$ For GDLs and void of catalyst layers: $S_v = \rho\vec{g} - \frac{\mu}{\tau_g}\varepsilon^2\vec{v} + \chi\kappa\frac{2\rho\nabla s_l}{(\rho_l+\rho_g)}$ For membrane: $S_v = \rho\vec{g} - \frac{\mu}{\tau_g}\varepsilon^2\vec{v} + \chi\kappa\frac{2\rho\nabla s_l}{(\rho_l+\rho_g)} + \frac{\tau_\phi}{\tau_p} c_f \eta_f F \nabla\phi_m$
Conservation of energy	For current collectors: $S_T = (I^2/\sigma_s)$ For gas flow channel: $S_T = r_w h_L$ For GDL: $S_T = \frac{I^2}{\sigma_s^{eff}} + r_w h_L$ For membrane: $S_T = \frac{I^2}{\sigma_m^{eff}} + r_w h_L$ For catalyst layer: $S_T = \eta R_{an,cat} + I^2\left(\frac{1}{\sigma_s^{eff}} + \frac{1}{\sigma_m^{eff}}\right) + r_w h_L$
Hydrogen transport	For anode catalyst layer: $S_{H_2} = -\frac{M_{H_2}}{2F} R_{an}$
Oxygen transport	For cathode catalyst layer: $S_{O_2} = -\frac{M_{O_2}}{4F} R_{cat}$
Water vapor transport	For anode catalyst layer: $S_{H_2O} = -\left(\frac{n_d M_{H_2O}}{F}\right) R_{an} - r_w$ For cathode catalyst layer: $S_{H_2O} = \frac{M_{H_2O}}{2F} R_{cat} + \left(\frac{n_d M_{H_2O}}{F}\right) R_{cat} - r_w$
Conservation of Charge	For anode catalyst layer: $S_{es} = -R_{an}$ $S_{em} = R_{an}$ For cathode catalyst layer: $S_{es} = R_{cat}$ $S_{em} = -R_{cat}$ For other parts: $S_{es} = 0$ $S_{em} = 0$

is solved for liquid water phase. The volume fraction of the gas phase is automatically computed based on the relative equation listed in Table 3

Energy conservation equation

$$(\rho c_p)_{eff}\frac{\partial T}{\partial t} + (\rho c_p)_{eff}(\vec{v}\nabla T) = \nabla\left(k_{eff}\nabla T - \sum_j h_j\vec{J}_j + (\tau\cdot\vec{v})\right) + S_T \quad (4)$$

The energy balance in terms of the temperature change was also considered. In the multi-phase model, the energy equation is also shared among the phases [26,27]. To specify parameters in the mixture including gas and liquid phases in porous media, the effective properties were determined (Table 3). The first three terms on the right-hand side of Eq. (4) represent energy transfer due to conduction taking place in solid and fluid zones, species diffusion, and viscous dissipation, respectively [26]. For the collectors what are pure solid materials, the species diffusion, viscous dissipation and convection term are negligible. For the channel and porous media, those three terms were considered since the fluid flow is presented in such regions. Note that the porosity specified in the energy equation determines different zones, depending on its values: 1 for the pure fluid zone (the channels), 0 for pure solid zone (the collectors and ribs), and between 0 and 1 for porous zones. The source term in the energy conservation includes heat from chemical reactions (only in the catalyst layers), Ohmic heating due to Ohmic resistance of solid zones, and phase change (condensation/evaporation processes). Hence, the sources terms of energy equation for different layers are different that listed in detail in Table 2.

Species transport equations

The species transport equations are generally in the following form:

$$\frac{\partial}{\partial t}(\varepsilon\rho Y_i) + \nabla\cdot(\varepsilon\rho\vec{v}Y_i) = D_{i,m}\nabla^2(\rho Y_i) + S_i \quad (5)$$

The model predicts the local mass fraction of each species, Y_i, through the solution of a convection-diffusion equation for the ith species, where $D_{i,m}$ is the diffusion coefficient for species i in the mixture shown in Table 3. The source term in the transport equation is shown in Table 2.

During the operation, the H^+ ions move from the anode to the cathode and also pull water molecules with their movement. This is known as the electro-osmotic drag effect. Physically, the water transport rate through the membrane from anode to cathode by electro-osmotic drag is computed as a function of volumetric current density and drag coefficient proposed by Springer et al. [28] for a Nafion membrane. In Springer's equation, the drag coefficient is defined to be a function of (the water content inside the polymer membrane). These parameters are listed in Table 3.

Conservation of charge

The current transport of electrons through the solid phase and ions through the membrane phase was represented by the following equations [26,27]:

$$\nabla\cdot(\sigma_s\nabla\phi_s) = S_{es} \quad (6)$$

$$\nabla\cdot(\sigma_m\nabla\phi_m) = S_{em} \quad (7)$$

The volumetric source terms S_{es} and S_{em} are defined as the volumetric transfer currents. The source term in the equation of charge is shown in Table 2.

The source terms representing the transfer currents were calculated by using Butler–Volmer equation [23]:

$$R_{an} = R_{an}^{ref}\left(\frac{C_{H_2}}{C_{H_2}^{ref}}\right)^{\gamma_{an}}\left[\exp\left(\frac{\alpha_{an,an}F\eta_{an}}{RT}\right) - \exp\left(-\frac{\alpha_{cat,an}F\eta_{cat}}{RT}\right)\right] \quad (8)$$

$$R_{cat} = R_{cat}^{ref}\left(\frac{C_{O_2}}{C_{O_2}^{ref}}\right)^{\gamma_{cat}}\left[\exp\left(-\frac{\alpha_{cat,cat}F\eta_{cat}}{RT}\right) - \exp\left(\frac{\alpha_{an,cat}F\eta_{an}}{RT}\right)\right] \quad (9)$$

The volumetric transfer current R is driven by the activation overpotential η, which is the potential difference between solid and membrane phases [26,27]. Note that the reference potential of the electrode V_{ref} is zero on the anode side and is equal to the open circuit voltage on the cathode side. The cell potential is then the difference between the cathode and anode solid phase at the terminal

Table 3
Physical, species, heat, mass and charge transport properties.

	Value/formulation
Physical parameter	
Mixture density	$\rho = s_l\rho_l + (1-s_l)\rho_g$
Volume fractions relation	$s_l + s_g = 1$
Mixture viscosity	$\mu = s_l\mu_l + (1-s_l)\mu_g$
Local mass average velocity of mixture	$v = \frac{s_l\rho_l v_l + s_g\rho_g v_g}{s_l\rho_l + s_g\rho_g}$
Effective volumetric heat capacity of porous media	$(\rho C_p)_{eff} = \varepsilon\rho_f C_{p,f} + (1-\varepsilon)\rho_s C_{p,s}$
Effective thermal conductivity of porous media	$k_{eff} = \varepsilon k_s + (1-\varepsilon)k_f$
Heat transport parameter	
Heat transfer rate due to forced convection	$\dot{Q}_{convection} = hA_s(T_s - T_\infty)(W)$
Heat generation rate for the fuel cell	$\dot{Q}_{generated} = I(1.25 - V_{cell})(W)$
Species transport parameter	
Water transport through the membrane by electro-osmotic drag	$\dot{m}_{H_2O} = \frac{n_d M_{H_2O}}{F} R_{cat}$
Drag coefficient	$n_d = (2.5/22)\lambda$
Membrane ionic conductivity	$\sigma_m = \varepsilon(0.514\lambda - 0.326)e^{1268((1/303)-(1/T))}$
Water content	$\lambda = 0.043 + 17.18a - 39.85a^2 + 36a^3 \quad (0 \le a \le 1)$ $\lambda = 14 + 1.4(a-1) \quad (1 \le a \le 3)$ $\lambda = 16.8 \quad (a > 3)$
Water activity	$a = \frac{P_W}{P_{sat}} = \frac{X_W P}{P_{sat}} + s_l$
Saturated pressure	$P_{sat} = 101325$ $*10^{(-2.1794+0.02953*(T-273.17)-9.1837*10^{-5}*(T-273.17)^2+1.4454*10^{-7}*(T-273.17)^3)}$
Species concentrations	$C_i = Y_i\rho/M_i$
Mass transport parameter	
Phase change rate (Condensation/Evaporation)	$r_w = c_r \max\left[(1-s_l)\frac{P_{wv}-P_{sat}}{RT}M_{H_2O}, -s_l\rho_l\right]$
Charge transport parameter	
Activation overpotential	$\eta = \phi_s - \phi_m - V_{ref}$
Cell potential	$V_{cell} = \phi_{s,cat} - \phi_{s,an}$
Average current density	$I_{ave} = \frac{1}{A}\int_{V_{an}} R_{an}d = \frac{1}{A}\int_{V_{cat}} R_{cat}d$

collectors (two ends of the cell collectors which are connected to the external electric circuit from both electrodes).

In order to satisfy the conservation of charge, the total current of either electrons or protons coming out from the anode catalyst layer must be equal to the total current coming into the cathode catalyst layer and must be equal to the total current caused by the proton movement through the membrane [28]:

$$\int_{V_{an}} R_{an}d = \int_{V_{cat}} R_{cat}d \tag{10}$$

2.3. Water transport and its effect on the properties of porous media

Water is formed in the cathode catalyst layer by electrochemical reactions—an amount of oxygen is consumed and an amount of water is produced. Due to the proton movement from the anode to the cathode through the membrane, water molecules are pulled with the protons by a force called electro-osmotic drag [26,29]. Additionally, water may diffuse through the membrane due to the concentration differences. The net water flux through the membrane results in a water balance between the electro-osmotic drag of water (from anode to cathode) and back diffusion (from cathode to anode)

$$J_w = J_w^{os} + J_w^{diff} = n_d\frac{M_{H_2O}}{F}\vec{I} - D_{i,m}\nabla(\rho Y_i) \tag{11}$$

In the present study, the membrane water diffusivity and membrane ionic conductivity were calculated by the expressions given by Springer et al. [28,29] and are listed in Table 3. It is almost a standard model and therefore the readers can check the original references for more details.

2.4. Volume of fluid (VOF) model

The VOF technique was implemented in the channels and porous media (including GDLs and catalyst layers) [26]. Interface between gas and liquid (two-phase flow) is tracked by the volume fraction of liquid water in the computational cell volume. In the VOF approach, the source terms of continuity and momentum equations used in the porous media include the effects of surface tension, wall adhesion and capillary water transport phenomenon.

2.4.1. Geometric reconstruction scheme

The geometric reconstruction PLIC scheme (piecewise linear interface construction) was employed because of its accuracy and applicability for general unstructured meshes, compared to other methods such as the donor–acceptor, Euler explicit, and implicit schemes. A VOF geometric reconstruction scheme is divided into two parts: a reconstruction step and a propagation step. Details can be found in [26,30].

2.4.2. Implementation of surface tension

The addition of surface tension to the VOF method is modeled by a source term in the momentum equation. The pressure drop

across the surface depends upon the surface tension coefficient χ [26]

$$\Delta p = \chi\kappa = \chi\left(\frac{1}{R_1} + \frac{1}{R_2}\right) \tag{12}$$

where χ denotes the surface tension coefficient, κ is the surface curvature; R_1 and R_2 are the two radii, in orthogonal directions, to measure the surface curvature. The surface tension force can be written in terms of the pressure jump across the interface, which is expressed as a volumetric force F added to the momentum equation

$$\vec{F} = \chi\kappa\frac{\rho\nabla s_l}{(\rho_l + \rho_g)/2} \tag{13}$$

where the term $(\rho/(\rho_1 + \rho_2)/2)$ is used to improve the Continuum Surface Force (CSF) method's capability of modeling surface tension in the case for fine meshes at high density ratio interfaces. This method is called "density-scaling of the CFS". It helps to maintain a constant interface thickness when the interface between a dense phase (namely, liquid water) and a light phase (namely, air) is tracked by using VOF algorithm [32]. The source terms for different regions of the fuel cell are given in Table 2. The surface curvature κ can be defined in terms of the divergence of the normal unit vector of the interface $\hat{n}$

$$\kappa = \nabla\cdot\hat{n} = \nabla\cdot(\hat{n}_{ss}\cos\theta_{ss} + \hat{t}_{ss}\sin\theta_{ss}) \tag{14}$$

where $\hat{n}$ is the unit vector normal to the interface between two phases near the solid surfaces, $\hat{n}_{ss}$ is the unit vector normal to the solid surfaces, $\hat{t}_{ss}$ is the unit vector tangential to the solid surfaces, and θ_{ss} is the static contact angle at the solid surfaces. For the electrode surfaces with different wetabilities, different static contact angles could be assigned, and different contact angles could result in different surface tensions ($\vec{F}$), thus influencing the water transport. The values of surface tension and contact angle used in this model are listed in Table 1.

2.4.3. Phase change

Liquid water is considered to appear in the fuel cell when the water vapor pressure reaches its saturated value at the cell operating temperature. Contrarily, liquid water is evaporated when the water vapor pressure is smaller than its saturated value. Water condensation and evaporation phase change is also an important factor to determine the presence of liquid water in multi-phase model. In the present study, the variation of water mass flow rate was due to condensation (or evaporation) as described in Table 3.

2.5. Boundary conditions

The summary of the boundary conditions is listed in Table 4. A brief description is provided below.

2.5.1. Inlet of flow channels

Inlet velocities, fuel and oxidant temperatures and mass concentration of species were set as given parameters listed in Table 4. Inlet velocities can be preliminarily calculated from the inlet flow rates based on the average current density (I_{avg}) and excess coefficient ω that is defined as

$$\omega_{H_2} = \frac{m_{H_2,supply}}{m_{H_2,consumption}}, \omega_{O_2} = \frac{m_{O_2,supply}}{m_{O_2,consumption}} \tag{15}$$

Then, inlet velocity expression is given by the following equations:

$$U_{H_2,in} = \omega_{H_2}M_{H_2}\frac{I_{ave}A_{surf}}{2F\rho_{H_2}A_{in}} \tag{16}$$

$$U_{O_2,in} = \omega_{O_2}M_{O_2}\frac{I_{ave}A_{surf}}{4F\rho_{O_2}A_{in}} \tag{17}$$

Table 4
Boundary conditions.

Locations of application	Boundary conditions
Inlet of the anode flow channel	$u = U_{an,in}$ $Y_{H_2} = Y_{H_2,in}$ $Y_{H_2O} = Y_{H_2O,an,in}$ $T_{an,in} = T_{H_2,in}$
Inlet of the cathode flow channel	$u = U_{cat,in}$ $Y_{O_2} = Y_{O_2,in}$ $Y_{H_2O} = Y_{H_2O,cat,in}$ $T_{cat,in} = T_{air/O_2,in}$
Outlet of the anode flow channel	$\frac{\partial u_{out,an}}{\partial x} = 0$ $\frac{\partial Y_{H_2}}{\partial x} = 0;\ \frac{\partial Y_{H_2O,an}}{\partial x} = 0$ $\frac{\partial T_{an,out}}{\partial x} = 0$
Outlet of the cathode flow channel	$\frac{\partial u_{out,cat}}{\partial x} = 0$ $\frac{\partial Y_{O_2}}{\partial x} = 0;\ \frac{\partial Y_{H_2O,cat}}{\partial x} = 0$ $\frac{\partial T_{cat,out}}{\partial x} = 0$
The anode terminal	$\phi_s = 0$ $\frac{\partial\phi_m}{\partial y} = 0$
The cathode terminal	$\phi_s = V_{cell}$ $\frac{\partial\phi_m}{\partial y} = 0$
External boundaries	$\frac{\partial\phi_s}{\partial x} = 0;\ \frac{\partial\phi_s}{\partial z} = 0;\ \frac{\partial\phi_m}{\partial x} = 0;\ \frac{\partial\phi_m}{\partial z} = 0$

2.5.2. Outlet of flow channels

The fully developed condition was assumed to be applied for the velocity field and species concentrations.

2.5.3. The terminal collectors

There were two terminal collectors in which the anode and cathode collectors were connected to the external electric circuit. It was necessary to determine the boundary conditions for phase potentials on these interfaces.

2.5.4. External boundaries

External boundaries are defined as all outside surfaces of PEMFC except the terminals (the outside surfaces of the current collectors where the current enters or departs from). The zero-current-flux condition was applied for the external boundaries due to no currents coming or leaving.

For the sake of simplicity, the cooling channel was not included in the present model. However, it is necessary to control the cell temperature. Consequently, the heat transfer was assumed to take place between the all outside surfaces and the ambient environment by forced convection. Note that heat is produced when the fuel cell operates. For the case in which water finally ends in vapor form, this heat generation rate is defined as a product of the total current and potential loss [31] (shown in Table 3). In order to ensure that the forced convection dissipates the heat converted from electricity, the following condition must be satisfied:

$$\dot{Q}_{convection} = \dot{Q}_{generated} \tag{18}$$

then the convective coefficient h was chosen as

$$h = \frac{I(1.25 - V_{cell})}{A_s(T_s - T_\infty)} \tag{19}$$

It should be noticed that it is necessary to have an estimated value of surface temperature, T_{surf}, of the fuel cell to calculate the convective heat transfer coefficient in Eq. (19). In this study, it was assumed that the temperature difference between the fuel cell surface and the ambient is about 50 °C when estimated the convective heat transfer coefficient.

Table 5
The grid properties of three different meshes.

Case No.	Type of channel	Geometrical dimension of the channel (m × m × m)	Number of grid cells	Grid size in the channel (m)
1	Straight	0.001 × 0.001 × 0.006	378,750	0.00004
2	Straight	0.001 × 0.001 × 0.006	42,000	0.0001
3	Straight	0.001 × 0.001 × 0.006	9,750	0.0002

2.6. Solution procedure

The above-coupled set of governing equations and relative equations were implemented into/Fluent® 6.2 by developing our own User-Defined-Functions (UDFs) based on the general Fluent package that does not include the PEMFC module developed by Fluent Inc. The developed UDFs are written in C language with about 2000 statements. For the computational grid used in this study, there were 279,500 grid cells in the computation domain of the interdigitated channel PEMFC employed to simulate the physical and electrochemical phenomena in the fuel cell. The VOF algorithm was employed to track the gas–liquid interface. The solution procedure for pressure–velocity coupling was based on PISO algorithm [33].

3. Results and discussion

3.1. Validation of grid dependency

The size of the mesh (grid resolution) evidently affects the accuracy of numerical solution. In other words, it was said that the results are related to the resolution of the numerical grid. Therefore, grid dependency would be done to check the solution at different grid sizes and get a range of the grid size in which the solutions are reasonably independent on the size of grid. In order to validate the grid dependency in this study, a very fine mesh with high resolution was applied to a straight channel fuel cell that has dimensions of 0.001 m × 0.001 m for channel cross-section and 0.006 m length of the channel and each cell in the straight channel has the same sizes

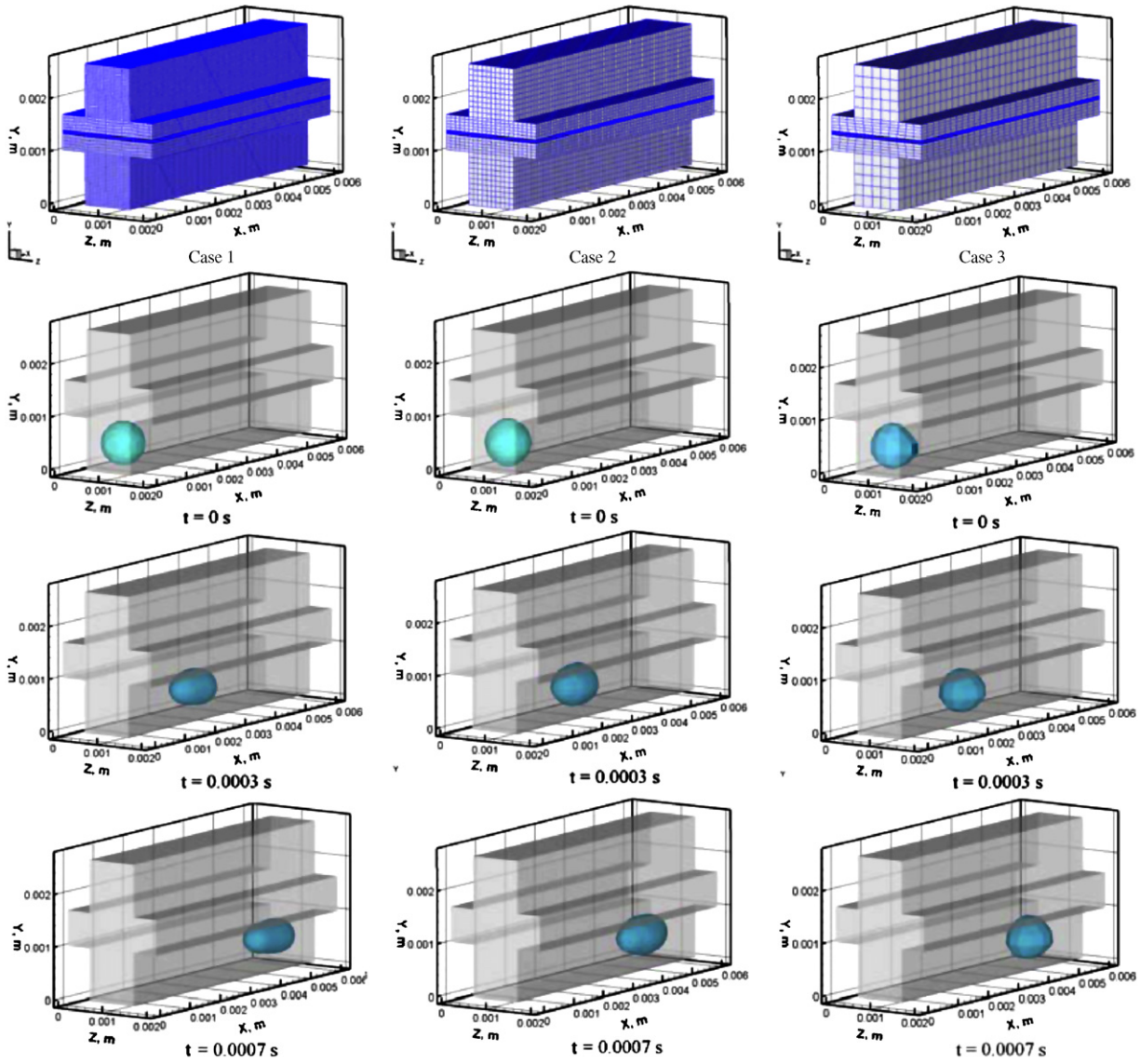

Fig. 2. Computational grids and comparison of liquid water tracking among three cases.

with 0.00004 m for three dimensions (Case 1 in Table 5). The computational domain of this mesh contains 378,750 cells. The other two coarser meshes were also generated on the same geometry of the straight channel with the number of computational cells of 42,000 (Case 2 in Table 5) and 9750 (Case 3 in Table 5). The geometrical and grid properties of the three cases are shown in Table 5 and Fig. 2. The coupling among two-phase flow dynamics, VOF interface tracking process and electrochemical reaction has been taken into account in the three cases. For solving fluid, heat, and mass transports equations coupled with VOF model and testing the possibility

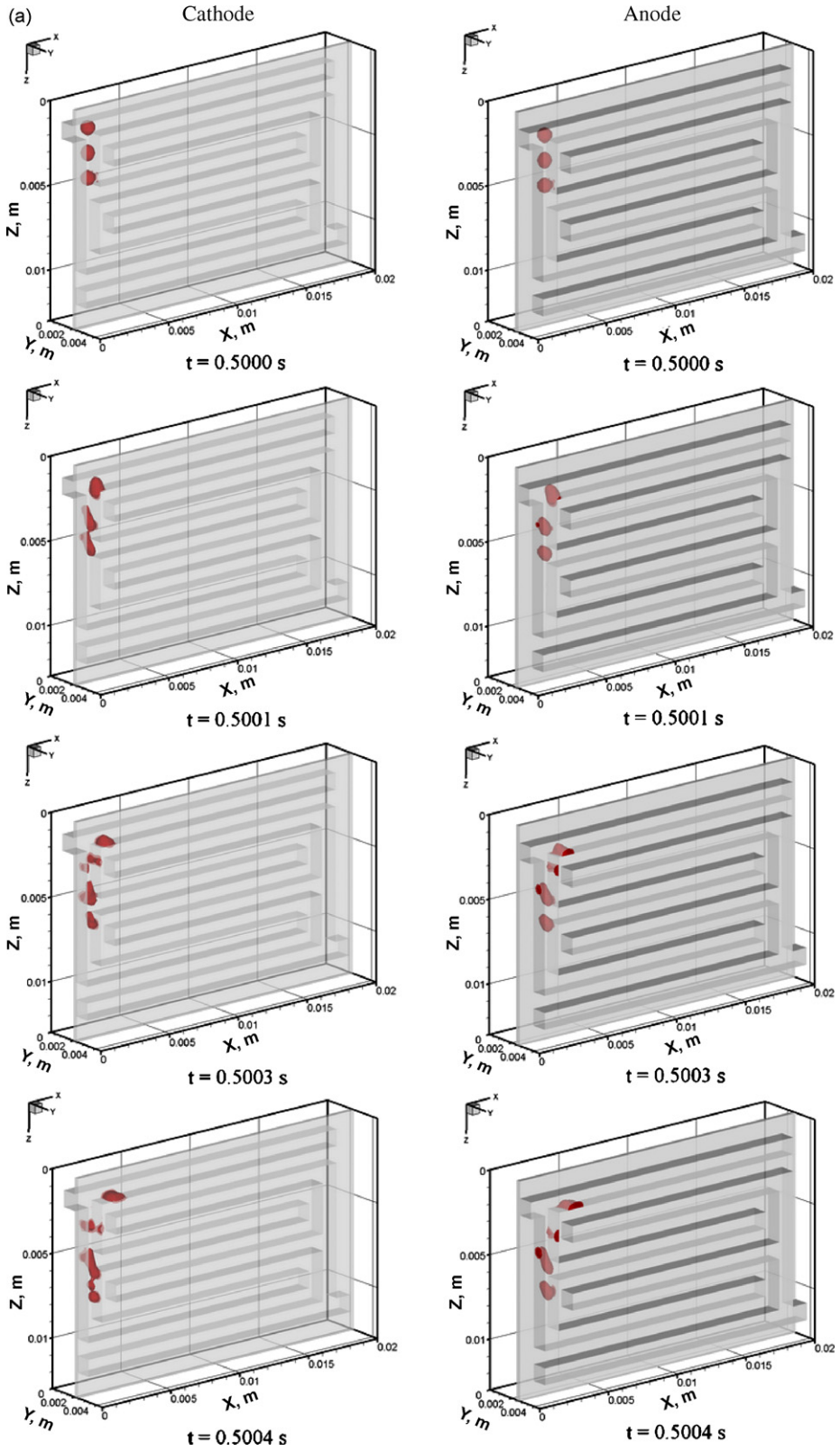

Fig. 3. Motion, deformation, detachment and coalescence of water droplets versus time in the cathode and anode: (a) from t = 0.50 to 0.5004 s, (b) from t = 0.501 to 0.504 s, (c) from t = 0.56 to 0.62 s and (d) t = 0.66 to 0.72 s.

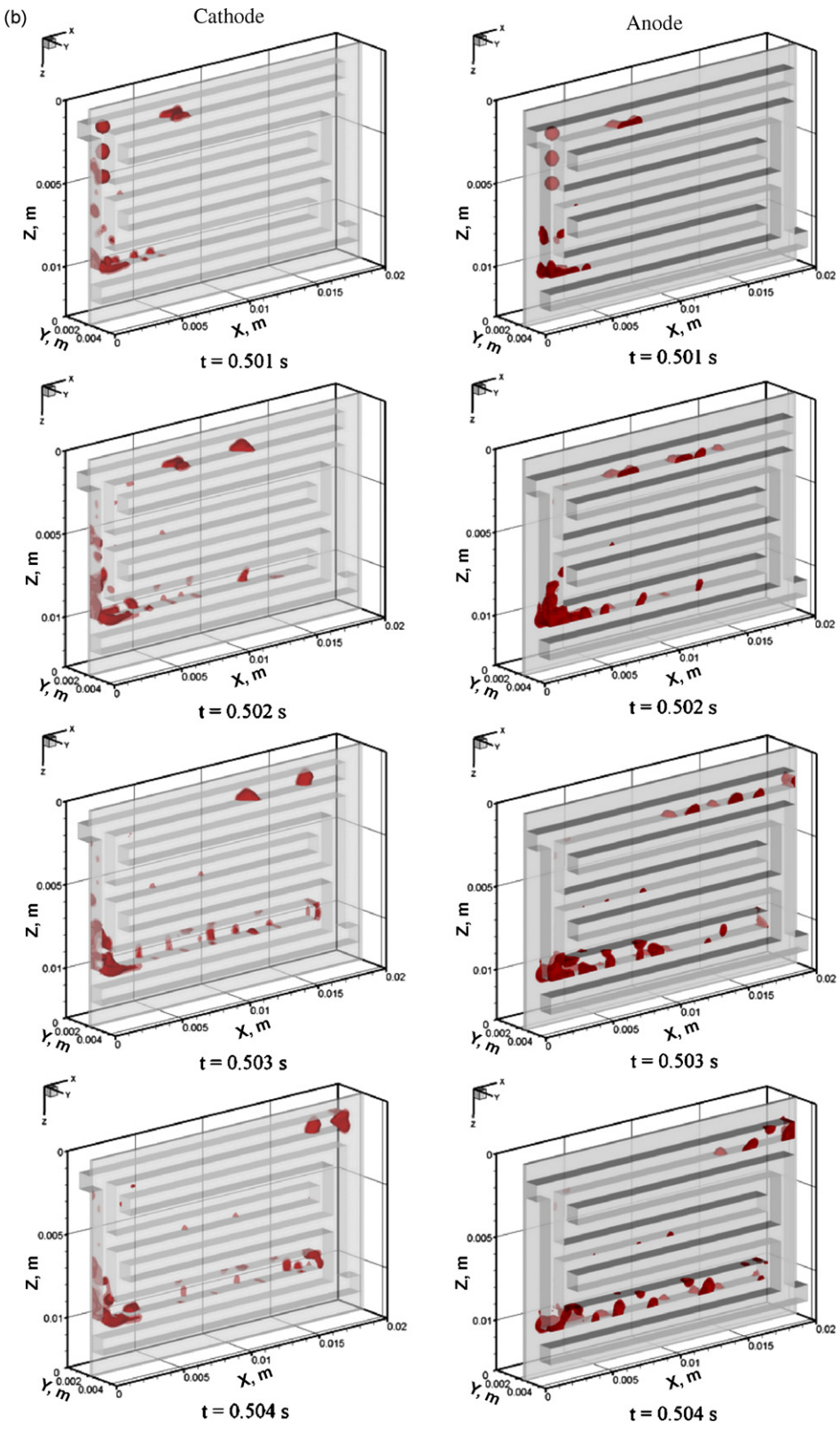

Fig. 3. (*Continued*)

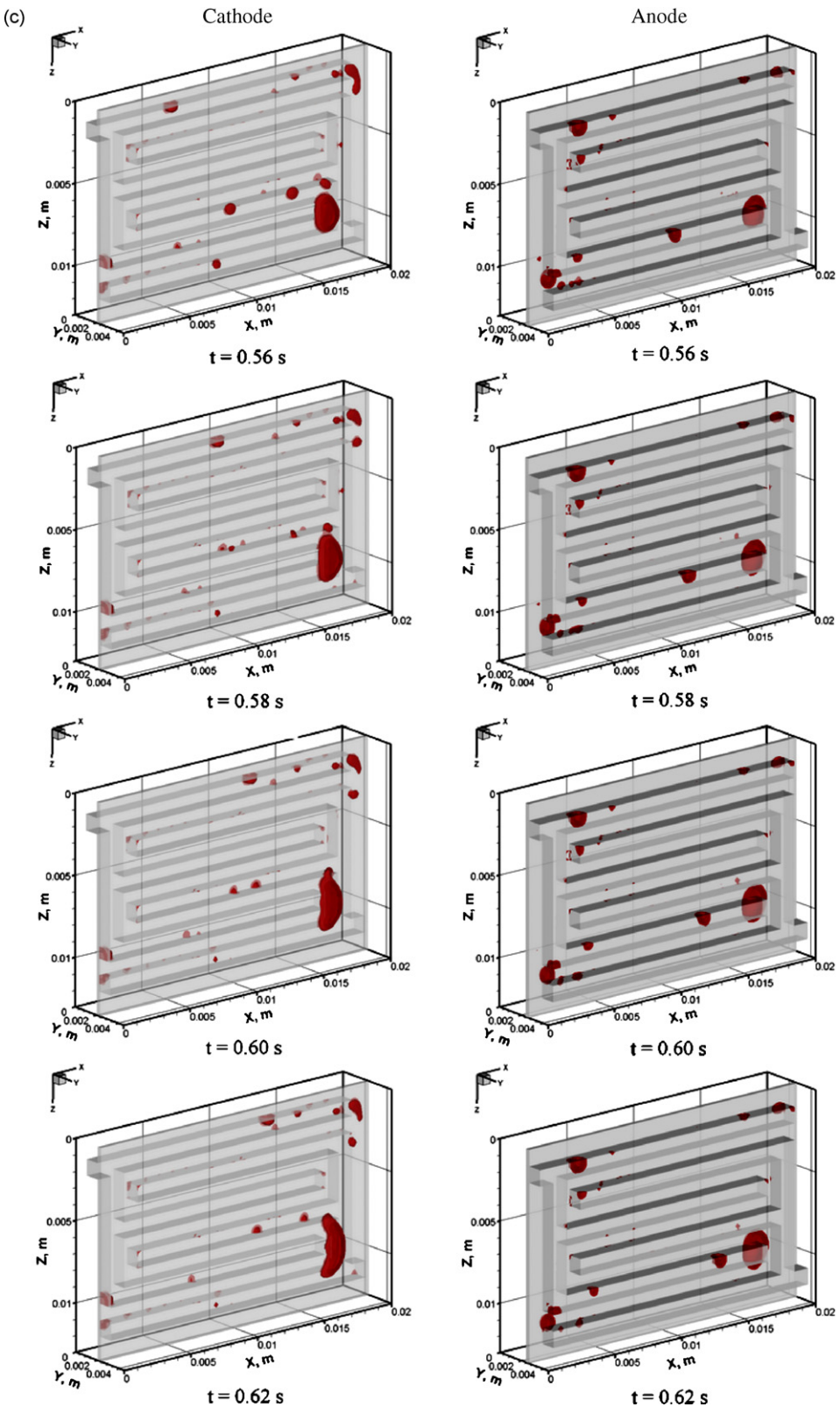

Fig. 3. (*Continued*)

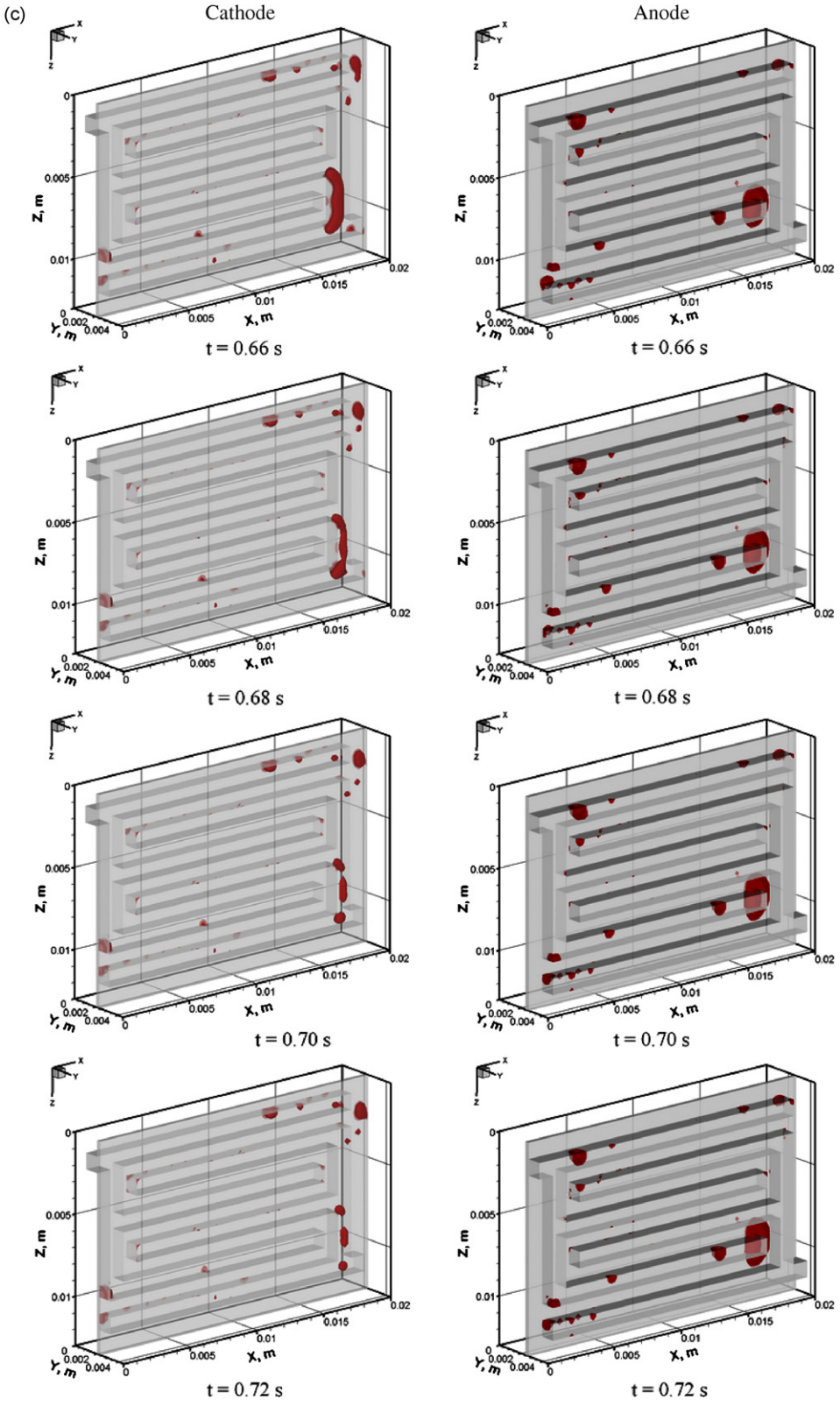

Fig. 3. (*Continued*).

of tracking liquid water inside the channel, a water droplet was initially added into the channel at the time $t = 0$ s. The time step used in the simulation for the three cases is 10^{-6} s. The simulation is considered to be completed when the water droplet moves out from the channel. In the three cases, the numerical results show that the motion and dynamic behavior of the water droplet can be investigated while the mass transport and electrochemical reaction are simultaneously taking place in the fuel cell as shown in Fig. 3. The results from these cases are quite similar in terms of the big picture of liquid water behavior. It also demonstrates that these meshes

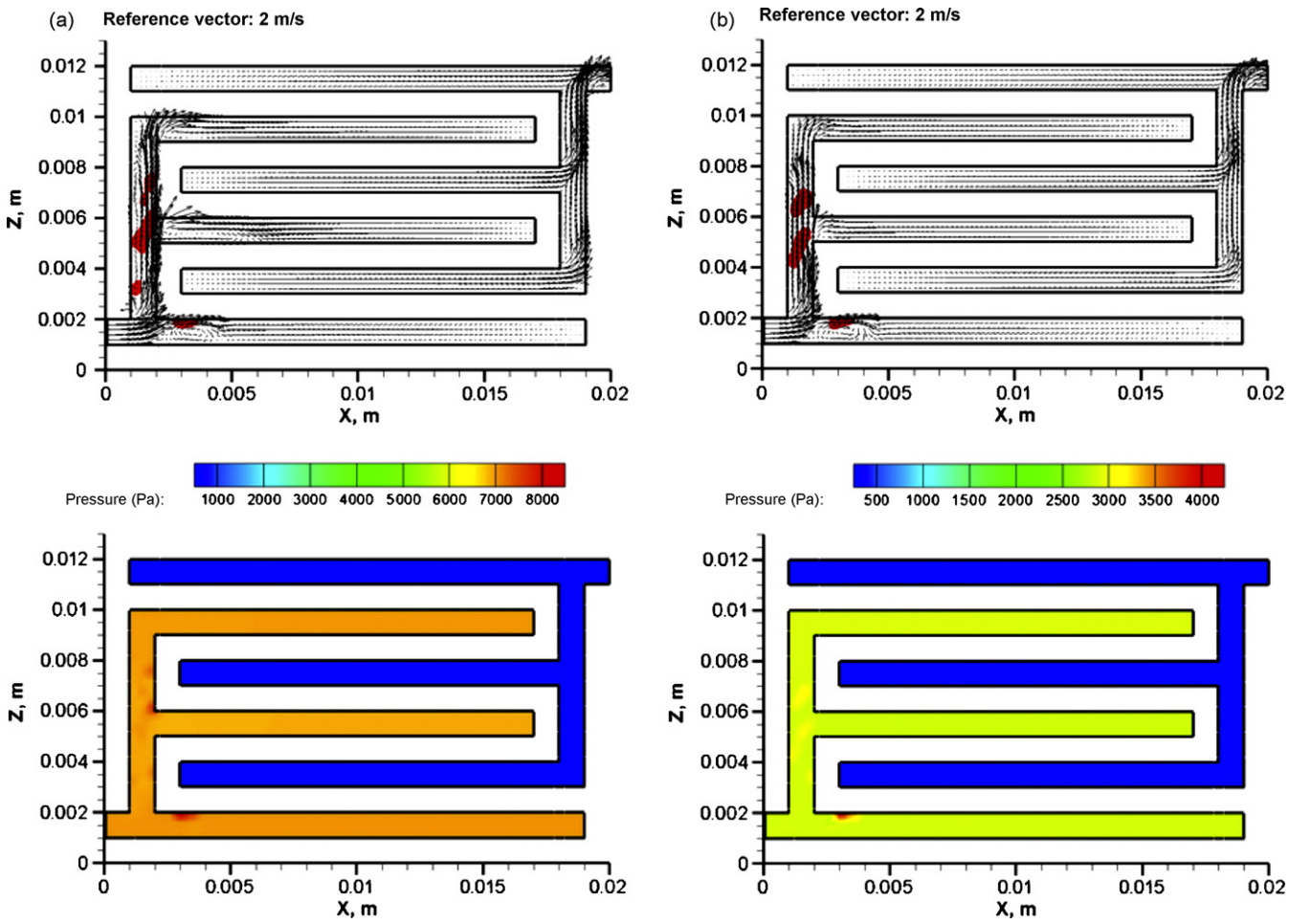

Fig. 4. Velocity vectors and pressure distributions at $t = 0.5003$ s: (a) on the middle-plane of cathode channel ($Y = 0.0015$ m) and (b) on the middle-plane of anode channel ($Y = 0.00317$ m).

with variation of number of grid cells (grid resolution) could be reasonable for solving the model.

However, it is noticeable that the maximum grid resolution that is practically feasible is limited by the available computational resource and time, especially if a large computational domain with complex geometry that is very popular in single fuel cell and fuel cell stack simulation is employed. For this reason, the coarser meshes are usually used if the solution is good enough to resolve the physical scales of the model. Hence, the grid size used in Case 3 would be applied on simulation of the interdigitated channel mesh in this study.

3.2. Analysis of liquid water movement in the channels and porous media

The effects of liquid water do not appear immediately but instead require time. The liquid water effects will become observable as water accumulates. Based on the experimental results, it usually requires at least several minutes of operation to make liquid water effects observable by naked eyes. In order to save the calculation time, an unsteady single-phase model was simulated from the time $t = 0$–0.5 s. To initialize the system, a series of liquid water droplets was suspended on both the anode and cathode channels at the time $t = 0.50$ and 0.501 s to further investigate two-phase flow behavior, especially the liquid water behavior across the porous media, together with the electrochemical reaction, heat and mass transfer. Due to the structure of the interdigitated channel, the gas and liquid water supply are forced under the bipolar plate and into the electrode, driving the water with it [31]. Therefore, liquid water transport and its effects would be entirely observed in the channels and porous media as well by implementing the VOF technique.

Fig. 3 shows the processes of motion, deformation, detachment and coalescence of water droplets versus time on both the cathode and anode channels and porous media at four sequential periods from $t = 0.50$ to 0.72 s. Initially, the droplets in spherical shape were added into the channel at $t = 0.50$ and 0.501 s (the positions of the initial droplets are shown in Fig. 3a).

3.2.1. From $t = 0.50$ to 0.5004 s (Fig. 3a)

Due to the droplet surface tension and shear stress from surrounding gas flow, the droplets were elongated downstream following the flow direction to the branches as time progressed. If the velocity gradients are large enough, the surface tension forces become unable to maintain the fluid particles intact, and thus it ruptures into smaller particles. Hence, after hitting the solid wall in the channels, these deformed droplets had the tendency to detach and then were broken into tiny deformed ones as slugs scattered on the wall surface. This period takes place in a short time due to high flow velocity in the channels.

3.2.2. From $t = 0.501$ to 0.504 s (Fig. 3b)

The small droplets sticking on the turning-wall would slowly move forward in the flow direction due to the effect of wall adhesion and surface tension while the other droplets from upstream are continuously approaching the turn, and further broken into the other smaller ones in the same way. At this moment, coalesce would

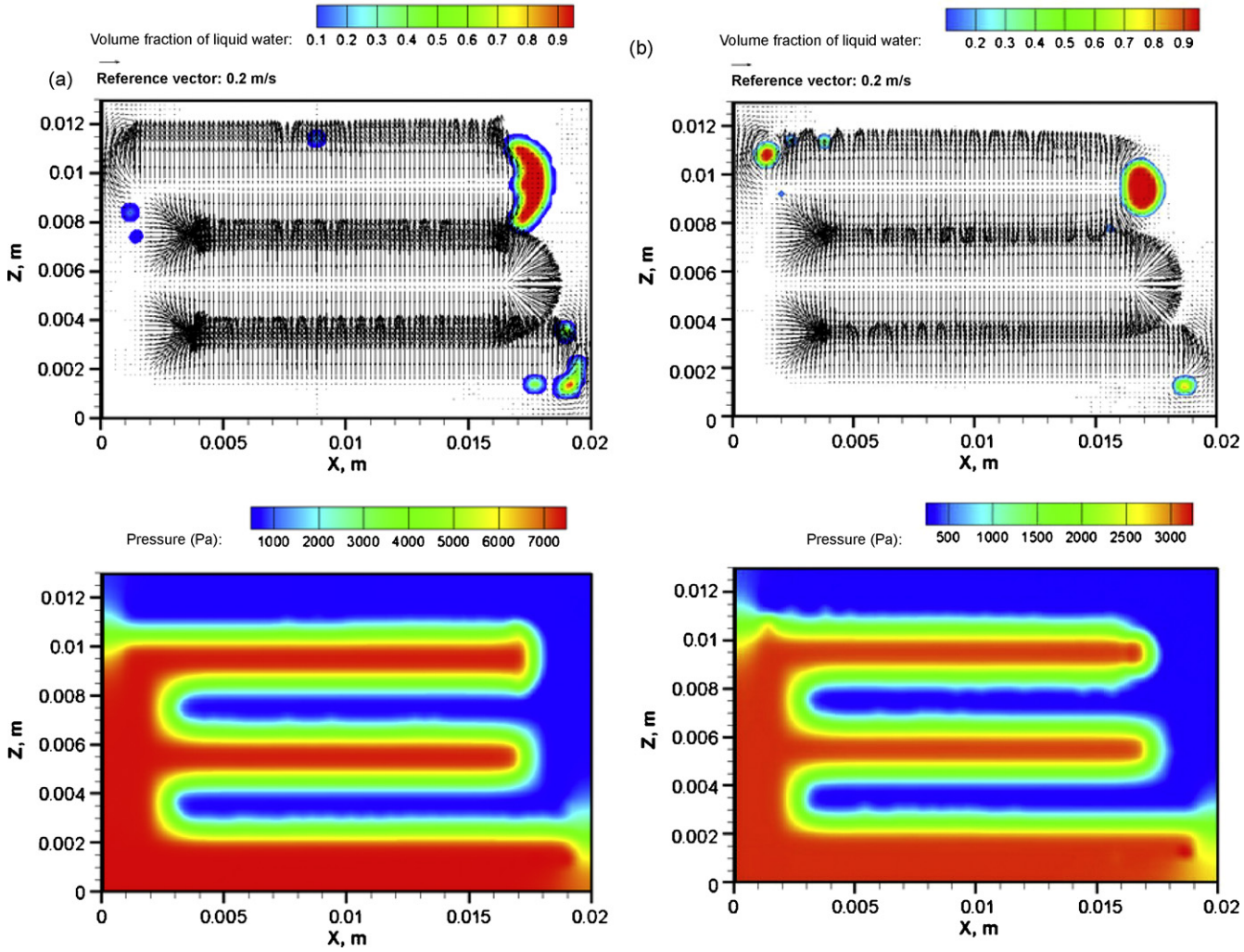

Fig. 5. Velocity vectors and pressure distributions at $t = 0.62$ s: (a) on the cathode GDL/catalyst layer interface ($Y = 0.0023$ m) and (b) on the anode GDL/catalyst layer interface ($Y = 0.00237$ m).

be presented in the droplets, making a high concentration of liquid water in the turning area. Consequently, the water droplet grows bigger. The shear stress due to the increasing air velocity through the blocked channel would increases and then pushes the water droplets downstream and elongates the droplets into "water bands" at the corners. However, these did not last long. Due to strong shear stress of the main flow in the straight channel, the water bands were broken again into the slugs that would gradually move to the end of the channels.

3.2.3. From $t = 0.56$ to 0.62 s (Fig. 3c)

At this period, the slugs gradually moved to the end of the channel, then built up at the regions under the channel-ends in both the cathode and anode porous media. Initially, the water slugs were pushed to the porous media from the channel by the secondary flow (the flow in Y-direction from the channel to the porous media applied for both the cathode and anode). In the porous media, those slugs were also strongly influenced by the primary flow (the flow in X–Z planes that is distributed in the porous media). For slugs in the porous media of an interdigitated channel, shear force caused by flow velocity dominates the removal. Depending on the flow velocity, the slugs would be deformed and spread to annular films in the cathode porous media or would keep their shape unchanged as slugs in the anode porous media. In other words, it can be said that the different velocity distributions of the gases would influence the formation of liquid water in the porous media. Note that the inlet velocity in the cathode is higher than that in the anode.

3.2.4. From $t = 0.66$ to 0.72 s (Fig. 3d)

In the cathode porous media, the water slugs were elongated by a strong shear force as the time progressed. This elongation was continued until the surface tension and wall adhesion was small than the shear force of the flow, then the slugs detached to smaller droplets ($t = 0.70$ s). Those droplets tend to be removed to the outlet channels by the gas flow and no longer appear in the cathode catalyst layer and thereafter, the GDL. In fact, liquid water removal is feasible in the porous media of the interdigitated channel in which the flow field was forced to pass through the porous media, resulting in strong convection in this region. In other types of flow channel such as serpentine, parallel or serpentine-parallel channels, the flow distribution in the porous media is usually much weaker when applying the same inlet mass flow rate or velocity. As a result, the liquid water is difficult to be removed in such types of channel PEMFCs. Even in the interdigitated channel with low inlet velocity (as the condition used for the anode channel of this PEMFC), the liquid water still remains unchanged in the porous media as shown in Fig. 2c and d from $t = 0.56$ to 0.72 s.

3.3. Velocity and pressure distributions under the presence of liquid water

3.3.1. In the channels

Fig. 4a and b presents velocity vectors and pressure distributions on the middle-plane of the cathode and anode channels (at $Y = 0.0015$ and 0.00317 m), respectively, at the time $t = 0.5003$ s. In the interdigitated channels, the flow field shown in those figures is in a maze with no outlet. The reactant gases are driven by the channel pressure, forced under the collector ribs and into the electrode. It can be clearly seen that the velocity vectors in the X–Z plane are highly distributed at the inlet, decreasing along the main channel to branches and getting very small at the channel cut (the end of the branches). The red contours indicate the liquid water that was deformed due to a combination of droplet surface tension and shear stress from surrounding gas flow. Therefore, the position and shape of deformed droplets distributed at the specific time are quite different based on the inlet velocities at the cathode and anode channels. In other words, the presence and blockage of water droplets over the channel led to the flow field distributing

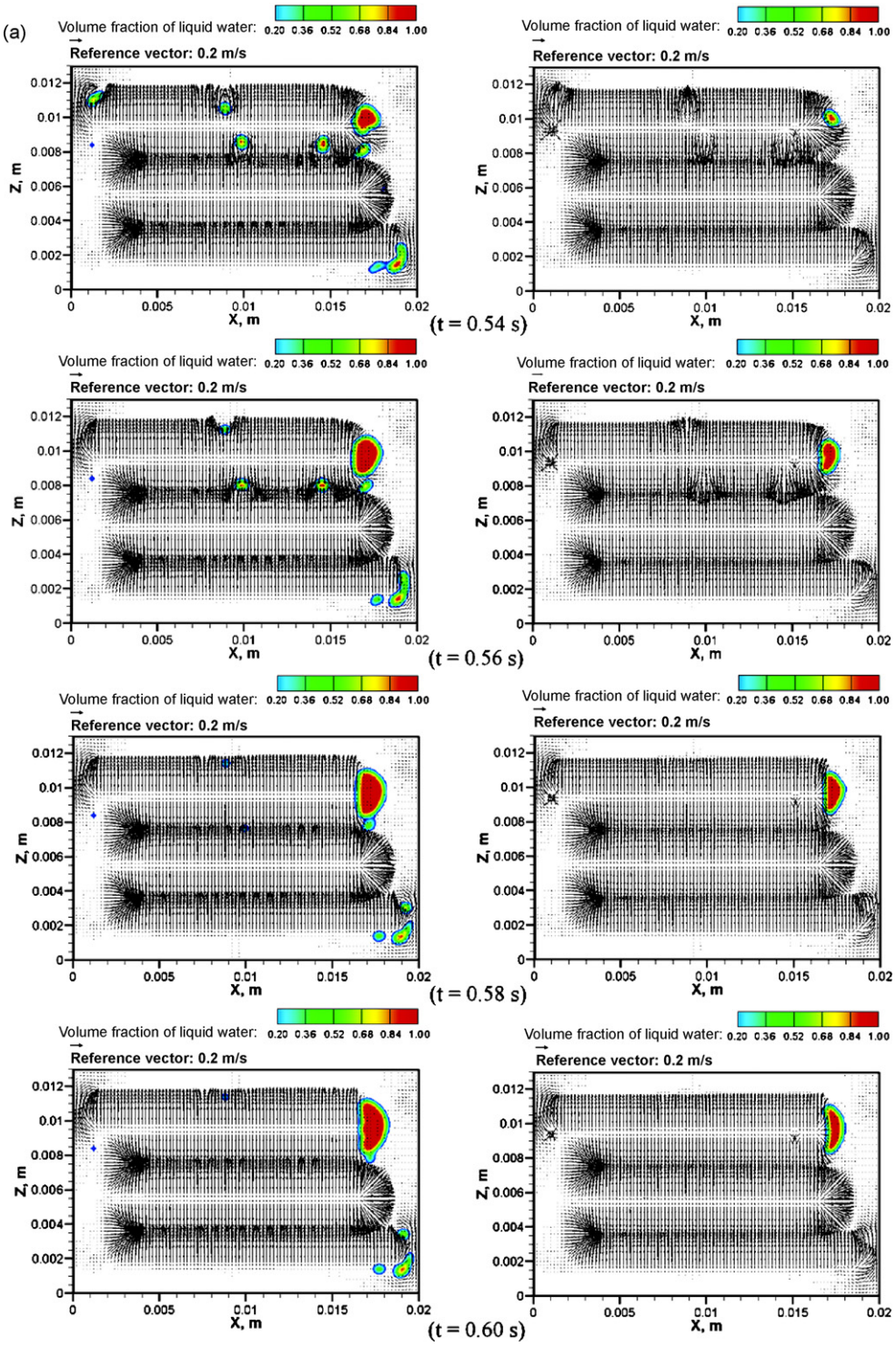

Fig. 6. Time evolution of the motion of liquid water in the cathode GDL and catalyst layer: (a) from $t = 0.54$ to 0.60 s and (b) from $t = 0.62$ to 0.68 s.

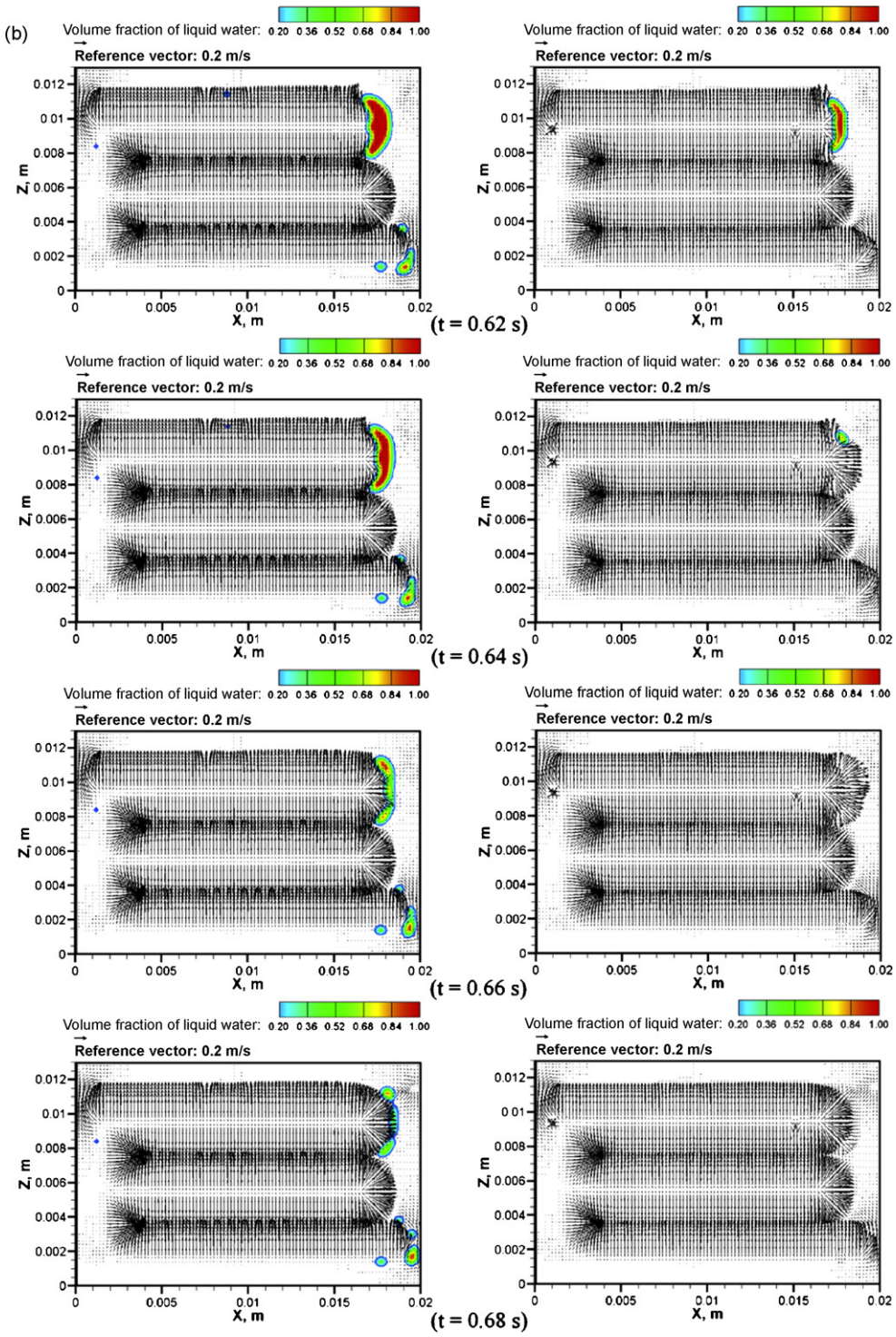

Fig. 6. (*Continued*).

in various ways, depending on where the droplets were located. In addition, pressure distributions in the interdigitated channels are insignificantly changed throughout the channel due to the fact that the flow resistance in the channel is very small compared with the resistance in the porous media. More interestingly, with the presence of droplets, the pressure drop reaches its highest values at around the location of the droplets due to the momentum resistance caused by the liquid water in the channel. It can be observed that the peaks of pressure coincided with the locations of droplets in the channel.

3.3.2. *In the porous media*

Liquid water is initially added into the channel, gradually moved in the channels and went through the porous media at the end of channel branches of both electrodes as shown in Fig. 3d. Similar to those in the channels, pressure and velocity distributions in the porous media are dramatically and insignificantly changed at the location where liquid water accumulates. Without the presence of liquid water, the velocity distributions in the porous media are influenced by the corresponding position of the interdigitated channel. Velocity vectors tend to go through the porous media from

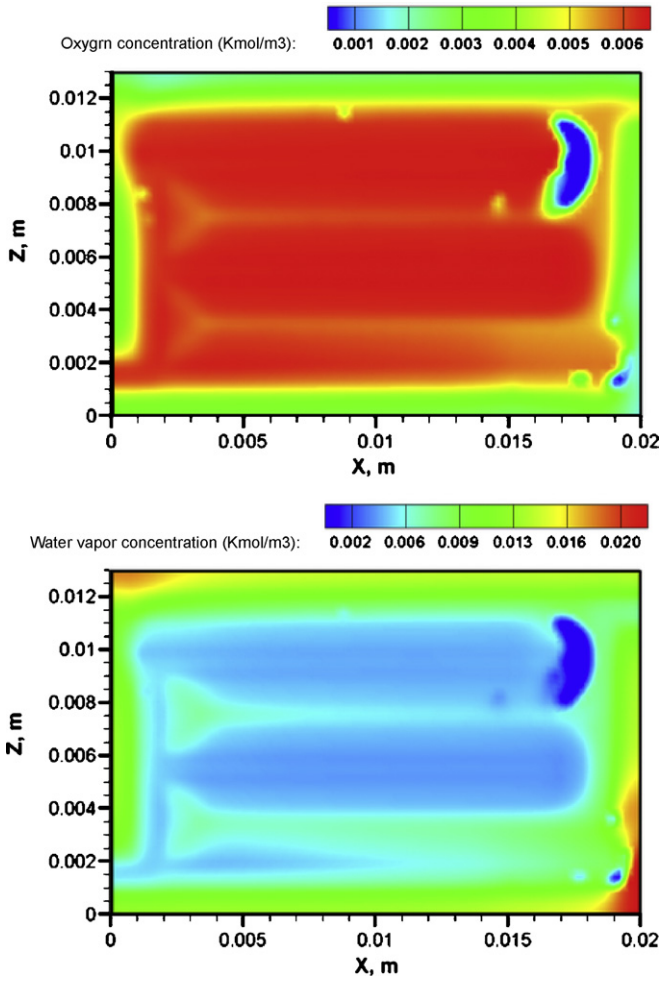

Fig. 7. Oxygen and water vapor concentration distributions on the cathode GDL/catalyst layer interface ($Y = 0.0023$ m) at $t = 0.62$ s.

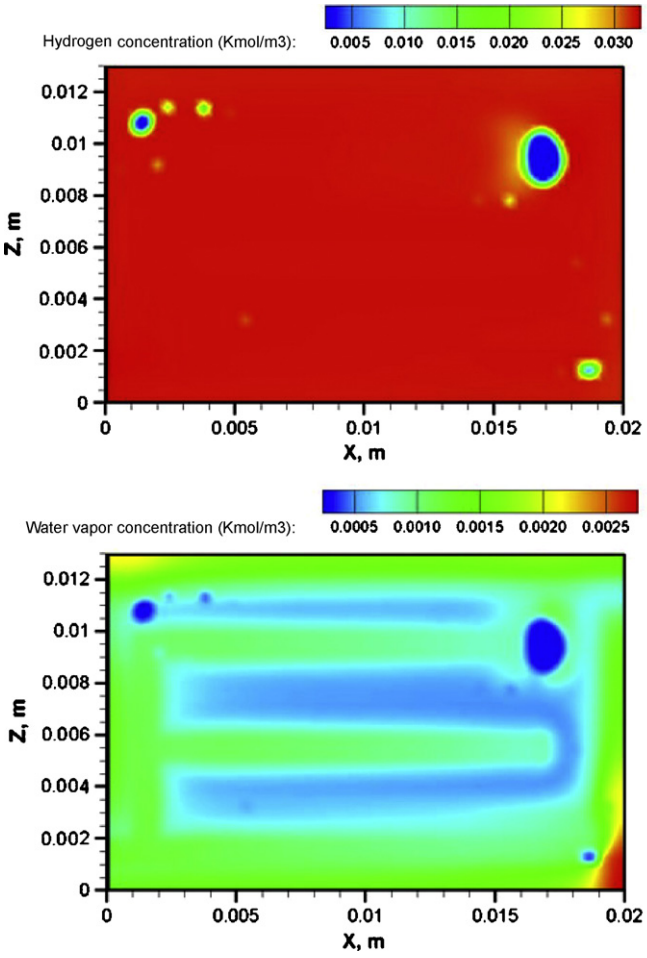

Fig. 8. Hydrogen and water vapor concentration distributions on the anode GDL/catalyst layer interface ($Y = 0.00237$ m) at $t = 0.62$ s.

the inlet channel to the outlet channel, such is a purpose of the interdigitated-shaped channel that mentioned above. However, it would be different if there was liquid water somewhere in the porous media. One can notice that unlike the channel, the velocity of the gas flow in the porous region is quite low (approximately at the order of 10^{-1} m s^{-1} or under), leading to a small shear stress that could not constrain the surface tension and adhesion of liquid water buildup in this region. In other words, it is likely that the liquid water in the porous media barrier of the gas flow, result in sudden changes of the flow distribution in the locations occupied by the liquid droplets, as shown in Fig. 5a and b. In addition, liquid water also causes a significant pressure drop inside the porous media. In fact, the pressure difference is a driving force that causes the reactant gases to flow through the GDLs and catalyst layers from the inlet channels to outlet channels. This difference would be much larger if the liquid water occupied somewhere in the flow field of the porous media blocks.

Fig. 6a and b shows the time evolution of the motion of liquid water in the cathode GDL and catalyst layer when a portion of liquid water emerges from the porous media. The gas flow from the channel drags liquid water towards the end of the channel branches and consequently pushes deformed droplets through the cathode GDL under the channel as seen in Fig. 6a at $t = 0.54$ s. It is noticed that most of the liquid water emerges from the porous media at the channel-end due to the fact that there is no flow exit of the inlet channel. As mentioned above, the gas flow velocity in the GDL is small due to porous resistance, hence decreasing shear stress acts on the surface of the water droplets. Intuitively, this shear stress seems to be much weaker than that in the channels. As a result, the growth and spread of water droplets in the porous media has a longer time evolution compared to the channels as shown in Figures from $t = 0.54$ to 0.66 s. In other words, the growth and spread of water droplets are quite slow in the GDL as well as the catalyst layer. In Fig. 6a and b, it also can be clearly seen that there is a large amount of liquid water concentrated in the region under the channel-end. Initially, liquid water is pushed from the channel to the porous media by the secondary flow in the Y-direction, the liquid water region is formed with a circular shape due to uniform velocity distribution. Furthermore, this region is influenced by the primary flow field distributed in the porous media (X–Z planes) instead of the secondary flow. The radial distribution of the flow velocity in the GDL region under the channel-end would make the liquid region deformed and elongated in the Z-direction as time progressed. Meanwhile, a small portion of liquid water in the GDL is pushed to the cathode catalyst layer by secondary flow in the cathode GDL, and also is deformed under the primary flow in the catalyst layer. The presence of too much liquid water in the GDL and especially in the catalyst layer would severely affect the fuel cell performance. A large amount of liquid water liquid should be somehow removed from the porous media to prevent flooding but a small amount should be kept to maintain a high conductivity of the membrane. Interestingly, the simulation results show that it is feasible to remove the liquid water by a high velocity field in the porous media of an interdigitated channel PEMFC as compared to the serpentine or parallel channel PEMFCs. The deformed liq-

uid water would continuously elongate until it is partially removed to the outlet channel. This is illustrated by a decrease of the volume fraction of liquid water in the liquid region shown in Fig. 6b at $t = 0.66$ s. It could be more clearly seen in the catalyst layer region that a large amount of liquid water first is pushed to the catalyst layer from the GDL at $t = 0.54$ s, then it is deformed and elongated under the impact of gas flow from $t = 0.56$ to 0.62 s, and eventually is taken away from the catalyst layer at $t = 0.64$ s.

3.4. Species concentration distributions in the porous media under the presence of liquid water

3.4.1. In the cathode GDL/catalyst layer interface

Fig. 7 shows the distributions of oxygen and water vapor concentrations on the cathode GDL/catalyst layer interface. The oxygen concentration is quite high in the porous region under the inlet and outlet channels and the area between the channels due to a strong flow convection in the region. Contrary to this, the oxygen concentration in the area adjacent to the edges is lower due to a low convection. It is realized that the flow field in the area near the edges is insufficient and the oxygen concentration is dominantly due to diffusion terms. Under the presence of liquid water inside the porous media, the oxygen concentration is significantly influenced. As shown in Fig. 7, there are few spots in the porous media that indicated low values of oxygen or water vapor concentrations. Undoubtedly, those spots represent the regions that were occupied by liquid water. The liquid water blocks the mass transport of gas species, resulting in a low concentration on the distribution of both oxygen and water vapor that were consumed and generated in the cathode catalyst layer, respectively. Interestingly, water vapor can be seen to be built-up in the area near the edges. It is the same phenomenon for the oxygen concentration, water vapor generated by chemical reaction in the catalyst layer is not easy to remove with a strong flow field in the area adjacent to the edges as discussed above in the previous section.

3.4.2. In the anode GDL/catalyst layer interface

Fig. 8 shows the distributions of hydrogen and water vapor concentration on the anode GDL/catalyst layer interface. Similar to the oxygen in the cathode, hydrogen is also considered as a reactant gas in the anode. However, the distribution of the hydrogen concentration in the interface is quite different from the oxygen in the cathode. Hydrogen seems to be evenly distributed on the interface regardless of the distribution of the flow field (convection effect) in the porous media. This can be clearly explained by the high diffusivity of hydrogen gas which causes the effect of convection on the hydrogen concentration to be negligible. The way that liquid water effects the hydrogen distribution is similar to that effects the oxygen distribution on the cathode GDL/catalyst layer interface. The build-up of water vapor in the area adjacent to the edges also can be seen in the anode catalyst layer and GDL. It is noticeable that the water vapor is supplied to the anode inlet as a humidifier and it would be dragged through the membrane from the anode to the cathode due to electro-osmotic drag force. The amount of dragged water depends on the reaction rate or in other words the current density. Therefore, it could not be doubted that the water vapor concentration in the porous region under the inlet and outlet channels and the area between the channels is lower than the other regions due to a high current density distributed in the region.

3.5. Temperature distribution under the presence of liquid water

Fig. 9 shows the temperature distributions on the cathode and the anode GDL/catalyst layer interfaces, respectively. The heat generation is due to the electrochemical reaction and Ohmic heating. Therefore, the temperature is proportional to the reaction rate,

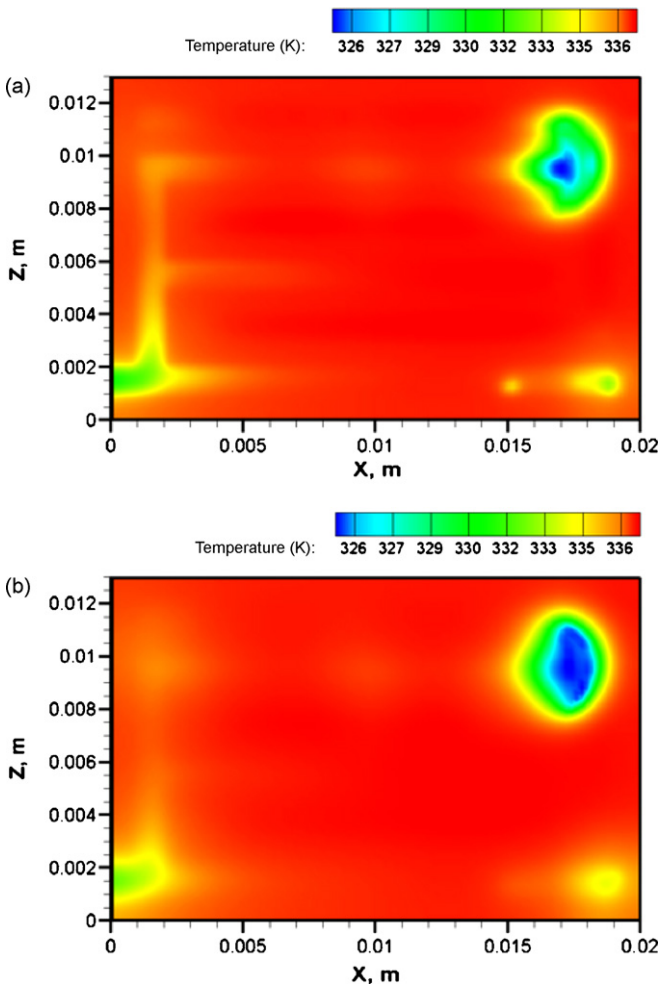

Fig. 9. Temperature distributions at $t = 0.62$ s: (a) on the cathode GDL/catalyst layer interface ($Y = 0.0023$ m) and (b) on the anode GDL/catalyst layer interface ($Y = 0.00237$ m).

which corresponds to the local current density distribution in the membrane (Fig. 11). Note that the heat transport in fuel cells is by diffusion, conduction and convection. The temperature distribution through the solid materials (including flow plates/collectors and solid phase of porous media) is also performed by the heat conduction process. Depending on different solid materials, the thermal conductivity may change, resulting in different temperature distributions in different solid layers. A uniform temperature distribution in the porous media is due to the high thermal conductivity of the solid material. However, the lowest temperature affected by convection could be observed at the flow inlet where the gas flows in at the ambient temperature. More interestingly, in the two-phase model, the presence of liquid water also affects the distribution of the cell temperature by absorbing heat from the cell, locally cooling down the temperature of the region where liquid water occupied, as seen in Fig. 8. As mentioned above, by controlling the convective coefficient h (Eq. (18)), the cell temperature distribution is in a good range of 325–337 °C.

3.6. Water content, water flooding and their effects on the current density distributions in the porous media under the presence of liquid water

Fig. 10 presents water content on the cathode GDL/catalyst layer interface. The water content is a function of water activity [29] which is the ratio of the water vapor pressure to the saturated pres-

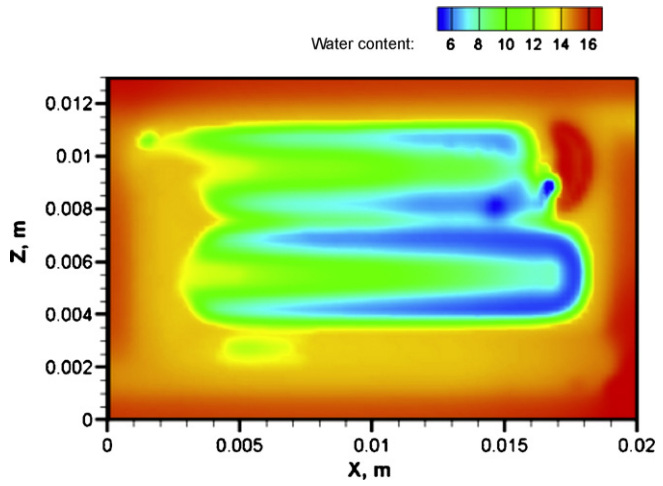

Fig. 10. Water content distributions on the cathode GDL/catalyst layer interface ($Y = 0.0023$ m) at $t = 0.62$ s.

sure. In the porous media, water content and ionic conductivity are strongly related. In general, the proton conductivity increases linearly with increasing water content. High water content in the porous media is desired to increase the conductivity and the current density as well. Similar to the distribution of water vapor concentration, it can be explained for the high water content in the porous media under the area adjacent to the edges and the low water content in the area under the channel in which water is taken away by forced convection. Contrary to this, the presence of liquid water severely directly influences on the current density by blocking the mass transport of reactant gas, restricting reactant availability and degrading the chemical reactions in the catalyst layers, resulting in a low current density distribution or performance loss where liquid water exists as seen in Fig. 11. Intuitively, Fig. 11 shows that the current density where the flooding occurs was observed at a value under 1000 A m^{-2}. Meanwhile, an average current density is valued at 6000 A m^{-2} and high values are over 7000 A m^{-2}. Furthermore, it can be noticed that the liquid water distribution in the porous media is not generally uniform and it might be easy to remove under a high convection due to the structure of interdigitated channel design. The removal of water from under the lands into the channel is essential to avoid flooding. However, a dry condition can result in low performance and durability. It could then be to trap liquid water somehow in order to humidify the porous media, especially in the anode. Hence, the interdigitated channel might have a limitation in keeping the liquid water for this purpose.

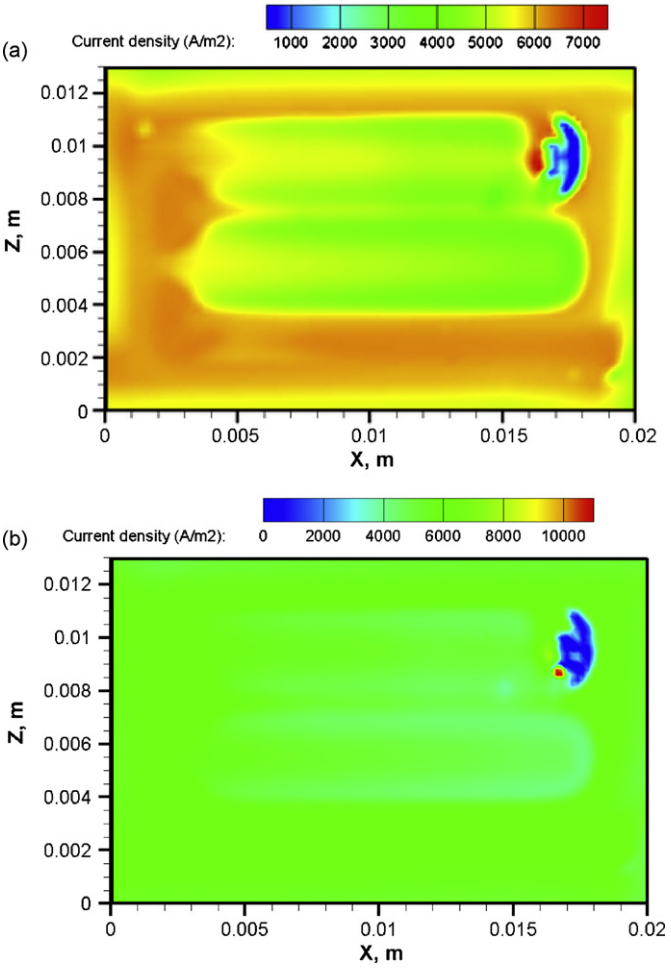

Fig. 11. Average current density distributions at $t = 0.62$ s: (a) on the cathode GDL/catalyst layer interface ($Y = 0.0023$ m) and (b) on the mid-plane of the membrane ($Y = 0.002335$ m).

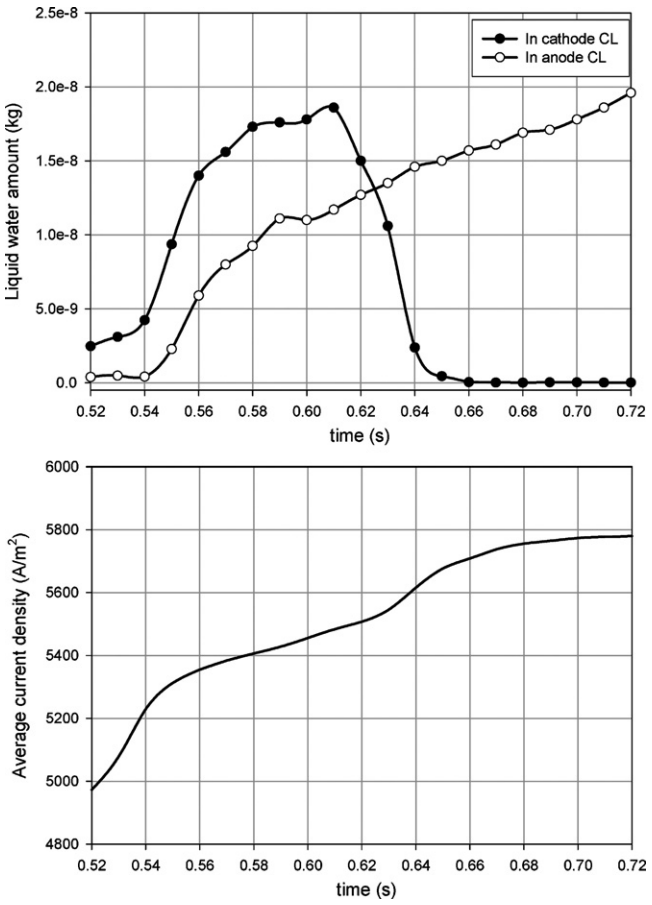

Fig. 12. Liquid water amount occupied in the cathode and anode catalyst layers and average current density variations with respect to time.

Fig. 12 shows the amount of liquid water present in the cathode and anode catalyst layers and the average current density with respect to time. The time evolution is taken from $t = 0.52$ to 0.72 s when the average current density starts to be stable until it nearly becomes constant. In the anode, liquid water seems to continuously penetrate to and build-up in the catalyst layer without removal as discussed in the previous section. In the cathode catalyst layer, this can be divided into three periods: liquid water penetrates to the catalyst layer ($t = 0.52$–0.56 s), liquid water accumulates in the catalyst

layer (t = 0.58–0.61 s) and liquid water is gradually removed from the catalyst layer (t = 0.61–0.72 s). Correspondingly, the average current density of the cell has changes due to the effects of flooding and the catalyst layer humidification. The average current density continuously increases during the three periods although the flooding has taken place in the cathode catalyst layer. It could be explained that the water vapor accumulated in the porous media by humidification and generation in the cathode, resulting in a high ionic conductivity of the catalyst layer and the membrane, and increasing the current density distribution over the active surface. The flooding, slightly influences the current density by degrading the rising slope of current density (as shown during the second period). In this case, however, it seems to be insignificant in terms of the cell performance.

4. Conclusion

In this study, the motion of water droplets in the channels and through the porous media has been investigated to give a good understanding of liquid water behavior including deformation, coalescence and detachment. The trace of liquid water in the channel and porous media was also predicted by analyzing the characteristics of liquid water and the influence of the interdigitated flow field on the liquid water distribution. Consequently, the numerical results of this model show that the presence of liquid water in the interdigitated channels and porous media directly and significantly influences flow field, species concentrations, heat and current transport. The main conclusions can be derived as follows:

1. A comprehensive 3-D, unsteady PEMFC model combined with a VOF interface tracking algorithm is a powerful and effective tool available for predicting the motion of liquid water in the channel and porous media of a PEMFC and investigating liquid water effects on the cell performance.
2. Liquid water removal is feasible in the channel and porous media of the interdigitated PEMFC. The reactant flow and transport to the channel and porous media in the interdigitated channel PEMFC is primarily subject to forced convection. Hence, this design effectively enhances the liquid water removal and forces the reactant flow to the GDLs and catalyst layers. The results show that the removal of liquid water strongly depends on the magnitude of flow field.
3. The presence of liquid water in the channel and porous media induces an uneven gas distribution and creates the high-pressure regions in which the liquid water occupies. As a result, this would provide inadequately distributed mass transfer to the catalyst layers and requires a high pressure supply for the fuel cell—in other words, it would consume more power for fuel cell operation.
4. By investigating the behavior of liquid water in the catalyst layers at different periods of time, it can be clearly observed that the liquid water blocks the gas transport in the fuel cell, resulting in a degradation of local current density. This severely affects the cell performance, especially when the flooding is significant.
5. The mass transport of reactant gas could be enhanced by forced convection in the interdigitated design, however the water vapor build-up inside the porous media under the collector ribs (between the inlet and outlet channels) can feasibly be taken away. Hence, this effect will reduce ionic conductivity of the porous media and eventually degrade the cell performance. This might be one of the main disadvantages of the interdigitated PEMFC design.

Acknowledgments

The authors are grateful for the support of this work by the Auto21™ Networks of Centers of Excellence (Grant D303-DFC), the Natural Sciences and Engineering Research Council of Canada (NSERC), the Canada Foundation for Innovation (CFI), the Ontario Innovation Trust (OIT), and the University of Windsor.

References

[1] H. Ju, H. Meng, C.Y. Wang, Int. J. Heat Mass Transfer 48 (2005) 1303–1305.
[2] H. Ju, G. Luo, C.Y. Wang, J. Electrochem. Soc. 154 (2007) B218.
[3] U. Pasaogullari, P. Mukherjee, C.Y. Wang, K.S. Chen, J. Electrochem. Soc. 154 (2007) B823.
[4] Y. Wang, S. Basu, C.Y. Wang, J. Power Sources 179 (2008) 603–617.
[5] S. Dutta, S. Shimpalee, J.W. Van Zee, J. Appl. Electrochem. 30 (2000) 135–146.
[6] Q. Ye, T.V. Nguyen, J. Electrochem. Soc. 154 (2007) B1242.
[7] B.R. Sivertsen, N. Djilali, J. Power Sources 141 (2005) 65–78.
[8] D.H. Schwarz, N. Djilali, J. Electrochem. Soc. 154 (2007) B1167.
[9] S. Mazumder, J.V. Cole, J. Electrochem. Soc. 150 (2003) A1510.
[10] M. Vynnycky, Appl. Math. Comput. 189 (2007) 1560–1575.
[11] J.H. Nam, M. Kaviany, Int. J. Heat Mass Transfer 46 (2003) 4595.
[12] B. Markicevic, A. Bazylak, N. Djilali, J. Power Sources 171 (2007) 706–717.
[13] J.I. Gostick, M.A. Ioannidis, M.W. Fowler, M.D. Pritzker, J. Power Sources 173 (2007) 277–290.
[14] O. Chapuis, M. Prat, M. Quintard, E. Chane-Kane, O. Guillot, N. Mayer, J. Power Sources 178 (2008) 258–268.
[15] U. Pasaogullari, C.Y. Wang, Electrochim. Acta 49 (2004) 4359.
[16] P. Quan, B. Zhou, A. Sobiesiak, Z. Liu, J. Power Sources 152 (2005) 131–145.
[17] K. Jiao, B. Zhou, P. Quan, J. Power Sources 157 (2006) 226–243.
[18] K. Jiao, B. Zhou, J. Power Sources 169 (2007) 296–314.
[19] X. Zhu, P.C. Sui, Ned Djilali, J. Power Sources 172 (2007) 287.
[20] X. Zhu, P.C. Sui, N. Djilali, Microfluid. Nanofluid. 4 (2008) 1613.
[21] X. Zhu, P.C. Sui, N. Djilali, J. Power Sources 181 (2008) 101.
[22] Z. Zhan, J. Xiao, M. Pan, R. Yuan, J. Power Sources 160 (2006) 1–9.
[23] P. Quan, M.C. Lai, J. Power Sources 164 (2007) 222–237.
[24] A. Golpaygan, N. Ashgriz, Int. J. Comput. Fluid Dyn. 22 (2008).
[25] A.D. Le, B. Zhou, J. Power Sources 182 (2008) 197–222.
[26] Fluent® 6.2 Documentation, Fluent Inc., 2005.
[27] C.S. Spiegel, Designing and Building Fuel Cells, McGraw-Hill, 2007, pp. 171–188.
[28] T. Springer, T. Zawodzinski, S. Gosttesfeld, J. Electrochem. Soc. 138 (1991) 2334.
[29] O'Hayre, Cha, Colella, Prinz, Fuel Cell Fundamentals, John Wiley & Sons, New York, 2006, pp. 93–136.
[30] C.S. Peskin, J. Comput. Phys. 25 (1997) 220.
[31] J. Larminie, A. Dicks, Fuel Cell Systems Explained, 2nd ed., John Wiley & Sons, England, 2003, p. 400.
[32] D.B. Kothe, W.J. Rider, S.J. Mosso, J.S. Brock, Volume Tracking of Interfaces Having Surface Tension in Two and Three Dimensions, AIAA 96-0859, 2006.
[33] H.K. Versteeg, W. Malalasekera, An Introduction to Computational Fluid Dynamics, John Wiley & Sons, 1995, p. 150.